Received 12 December 2024; accepted 5 January 2025. Date of publication 16 January 2025; date of current version 26 March 2025.

Digital Object Identifier 10.1109/OJAP.2025.3530251

A Design Method to Increase the Bandwidth of Reflectarray Antennas

CHRISTOS EXADAKTYLOS (Graduate Student Member, IEEE), ANASTASIOS G. KOUTINOS (Member, IEEE), CONSTANTINOS L. ZEKIOS (Senior Member, IEEE), AND STAVROS V. GEORGAKOPOULOS (Senior Member, IEEE)

Department of Electrical and Computer Engineering, Florida International University, Miami, FL 33174, USA

CORRESPONDING AUTHOR: C. L. ZEKIOS (e-mail: kzekios@fiu.edu)

This work was supported in part by the National Science Foundation under Grant ECCS 2127762, and in part by the Air Force Office of Scientific Research under Grant FA9550-19-1-0290 and Grant FA9550-23-1-0386.

ABSTRACT This work introduces a novel design methodology to redesign traditional reflectarray antennas (RAs) with bandwidths in the order of 15% and double their bandwidth without increasing their design complexity. A wideband RA unit cell (UC) is designed utilizing multiple connection points between the radiating and phase shifting structure. Notably, to properly set the desired phase shift at each UC of the RA aperture across the entire frequency band, true-time-delay (TTD) lines are connected to each element. To validate the performance of our proposed approach a traditional microstrip patch-based RA is used as an example. By applying our proposed method to this RA, we develop a design that achieves a fractional 1.5 dB gain bandwidth of 31% (8.6 GHz to 11.8 GHz) in the X-band, which is more than two times larger than the 14% fractional bandwidth of the traditional RA design. Our RA is prototyped to validate its performance. The measurements show excellent agreement with simulations thereby validating our proposed methodology.

INDEX TERMS High-gain antennas, reflectarrays, bandwidth enhancement, frequency pulling technique, true-time-delay.

I. INTRODUCTION

REFLECTARRAY antennas (RAs) [1] are a well-established solution for high-gain antenna applications. They are known for combining the advantages of reflector antennas (i.e., high gain, large apertures) with those of phased array antennas (i.e., beamsteering, low profile) [2], [3], and they are implemented in both fixed [4] and steered [5] beam applications for terrestrial (e.g., used in 5G base stations) as well as satellite communications [6]. However, the operation of RAs is constrained by their inherently narrow bandwidth (BW) (e.g., [7], [8]). This limitation arises from two main factors: (a) the use of narrowband antenna elements, such as microstrip patches (e.g., [9]), and (b) the differential spatial phase delay introduced by the various propagation paths from the feed phase center to each RA unit cell (UC) (e.g., [10]).

In the literature, a wide variety of reflectarray designs can be found, employing various radiating structures and corresponding phase-shifting methods used to compensate for the differential spatial phase delay discussed above. Single-layer designs are prevalent, due to their reduced design complexity and fabrication ease. In such cases, the variable patch size technique is commonly used for phase shifting (e.g., [11]). For example, Mao et al. in [12], utilized the variable size technique combined with optimization methods on an RA aperture loaded with square rings achieving a 16% fractional bandwidth, while Chen et al. [13], applied the variable size technique on circular elements with slots to achieve a 22.7% bandwidth. Additionally, Guo et al. [14], demonstrated an RA based on sub-wavelength ring patch elements, increasing the bandwidth to 29%. Min and Guo [15], demonstrated similar bandwidth performance by using a slotted rectangular patch with concave arms, achieving a fractional bandwidth of 32%. Li et al. [16], introduced spiral dipole elements and square rings on the same plane slightly increasing the fractional bandwidth to 35%. Moreover, Su et al. [17], demonstrated an RA with a bandwidth of 35%, utilizing circular cosine curve elements. However, all the RA designs

in [14], [15], [16], [17] include complex shaped patch elements with closely spaced features (i.e., copper traces) in their UCs, leading to increased complexity and limited scalability to higher operational frequencies. Similar to traditional microstrip antenna design, several techniques have been employed to enhance the bandwidth of RAs, often at the expense of radiation efficiency, antenna profile, or fabrication ease. For example, Encinar [18], used dual stacked patches to demonstrate an RA with a bandwidth of 16.7%. Li et al. [19], used a fixed-size circular ring loaded with a variable-length open-circuited stub and significantly increased their RA's profile by placing their design over a grounded thick foam substrate to achieve a bandwidth of 17.8%.

A different approach to increase the bandwidth of RAs is the use of true-time-delay (TTD) lines to apply the required phase delay at each radiating element. This is commonly achieved by using transmission lines (TLs) connected to the desired RA elements (e.g., [20]). Such RAs can demonstrate wide bandwidths in the order of 15%, and even wider when TTD lines are connected to wideband elements. For example, Carrasco et al. in [21] and [22], proposed a wideband RA based on patches aperture coupled to microstrip lines achieving more than 10% and 26% element and RA bandwidths, respectively. Even ultra-wide bandwidths in the order of 5:1 can be achieved when ultra-wideband antenna elements are connected to TTD lines [23]. However, such designs sacrifice aperture efficiency over bandwidth. For example, in [23], an aperture efficiency of approximately 15% was attained across its 5:1 bandwidth. An alternative method to apply TTD is using block-based unit cells with variable heights. In this manner, the propagation path length and equivalently the acquired reflection phase of each UC is controlled to form a highly focused beam. This phase shifting method is geometric and non-resonant, while even TTD phase compensation can be applied at the cost of increased profile. For example, in [24], a wideband full-metal RA with a bandwidth of at least 22.5% was demonstrated. The unit cell had the form of a metallic block of variable height. Similarly, Cao et al. [25], designed a full-metal RA based on metallic block elements with double-stage notches etched on them, achieving a fractional bandwidth of 17.6%. A similar architecture was employed in [26] for a block-based RA with dielectric waveguide elements of variable height, resulting in a bandwidth of 18%. Although, the block-based RAs in [24], [25], [26] can result in wide gain bandwidths, they are characterized by high RA profiles. Moreover, their profile increases with the aperture size, i.e., greater aperture size is equivalent to greater required phase range, resulting in even higher profiles when high gain is required.

It is well established from the above example references that a tradeoff between various performance metrics (i.e., profile, efficiency, or complexity) needs to be made in order to increase the bandwidth of RAs. Therefore, an important research question to investigate is: "Can the bandwidth of conventional RAs be increased while maintaining a low profile, high efficiency, and low fabrication complexity?". In this work, we answer this question by introducing a new design method for RAs to increase their bandwidth. Specifically, we redesign RA unit cells by connecting them to phase-shifting structures at multiple points utilizing the frequency pulling technique (FPT), [27], and TTD line concepts. The FPT is a recently introduced technique used to increase the BW of antenna elements, [28], [29], [30] while TTD lines are a well-established solution for systems that require wideband beamforming. To validate our proposed design methodology, an RA based on dual-fed[1] patch elements is designed and compared to its traditional counterpart with single-fed[2] elements. The patch elements are connected to TTD mictrostrip lines, which are placed below the ground plane of the patches. In [31], a preliminary analysis of this work can be found. However, our results, in [31], demonstrated a high gain variation of 3 dB and a low minimum aperture efficiency of 15% within the enhanced 30% RA bandwidth due to the phase errors introduced by the single-meandered delay line that was used for beamforming. Here, we achieve a stable gain response with a variation of only 1.5 dB and a minimum aperture efficiency of 30% for a fractional bandwidth of 31%. This bandwidth is more than two times greater than the 14% of fractional bandwidth achieved by the corresponding traditional RA with the single-fed UCs. Notably, using our design methodology, we increase the RA bandwidth, while preserving low profile, high efficiency, and low fabrication complexity as it will be established in the next sections.

The rest of the paper is structured as follows. In Section II, our design methodology of wideband RAs is presented. Section III demonstrates how our proposed methodology is utilized to design a novel dual-fed patch UC with increased BW, while Section IV shows the design of an RA aperture based on our novel UC as an example. In Section V, we compare the simulated performance of our RA, which is based on dual-fed patches, with the performance of a traditional RA that uses single-fed patches. Consecutively, in Section VI, the fabricated RA, measurement setup, and potential measurement errors are presented. In Section VII, the measured results along with the corresponding simulated ones are shown and analyzed. In Section VIII, a comparison of our proposed example RA with other relevant state-of-the-art RA designs from the literature is conducted. Finally, Section IX concludes our work.

II. PROPOSED DESIGN METHODOLOGY

As discussed in Section I, traditional RA designs typically fall into one of two categories: (a) low-profile and easy to fabricate but limited to an average fractional bandwidth of 10%, or (b) bulky with increased design complexity but capable of reaching average bandwidths of 30%. These characteristics largely stem from the conventional design methods

[1]The term dual-fed is used to describe reflectarray unit cells with two connection points between the radiating and phase-shifting structure.

[2]The term single-fed is used to describe reflectarray unit cells with one connection point between the radiating and phase-shifting structure.

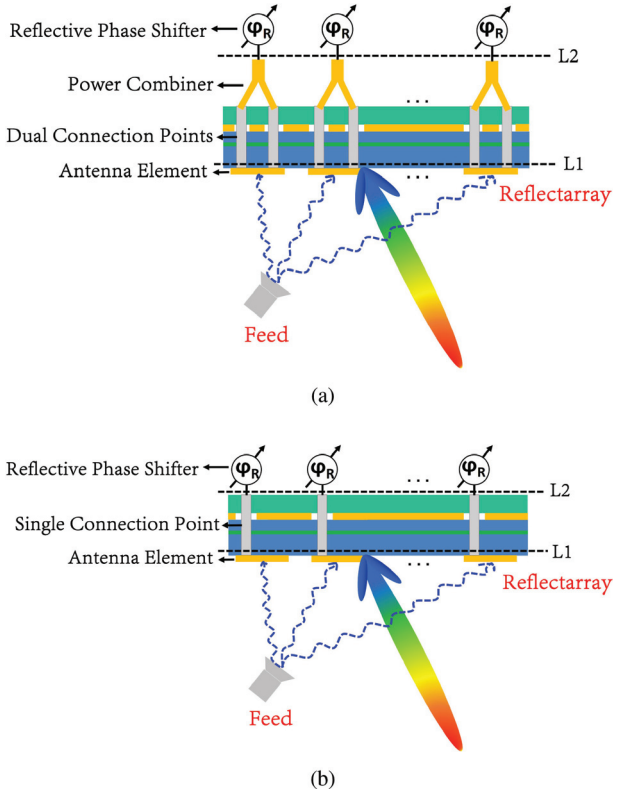

FIGURE 1. Schematic of (a) RAs designed with our proposed method, and (b) conventional RAs.

employed in prior works (see Fig. 1(b)). In this work, we introduce a novel design methodology (see Fig. 1(a)), that addresses the challenge of designing wideband RAs while maintaining a low profile, high efficiency, and low fabrication complexity. Our design methodology follows two steps: (a) the implementation of an unconventional dual-point connection mechanism for the radiators, and (b) the use of true-time-delay lines.

In traditional RAs, a spatial feed (e.g., a horn antenna) illuminates the RA aperture, and the radiated electromagnetic (EM) wave is received and reflected by each RA element. Typically, to compensate for the differential spatial phase delays caused by the various propagation paths from the feed phase center to each RA unit cell, methods such as varying the size of patch radiators or the length of transmission lines connected to the radiators have been used. Our approach employs transmission lines to provide TTD performance, offering a significant advantage in bandwidth over the variable patch size technique. Unlike conventional TTD-based designs, which typically connect the antenna element of each unit cell to a single point on the transmission line as shown in Fig. 1(b), our method adopts a unique dual-connection point scheme (see Fig. 1(a)). Specifically, we select two connection points on each RA element and by utilizing the FPT methodology, we design a power combining network that strategically connects these two points to a single one. At this junction, a TTD transmission line is attached, serving as the reflective phase shifter, shown in Fig. 1(a). Once the appropriate phase is achieved, the EM wave follows the inverse path, being re-radiated by each RA element to form a focused beam in accordance with array theory [32]. By employing the FPT, we significantly broaden the frequency range over which good impedance matching is maintained between the antenna element (L1 in Fig. 1(a)) and the phase shifter connection point (L2 in Fig. 1(a)), thereby enhancing the overall bandwidth of the RA. Notably, to significantly enhance the BW of the RA, it is essential to combine the TTD lines with the FPT. Specifically, the TTD lines provide the required phase distribution with minimal to no phase errors regardless of the frequency, meaning that TTD lines support, in theory, infinite bandwidth. Meanwhile, the FPT effectively extends (i.e., nearly doubles in this work) the bandwidth over which the patch efficiently transfers the EM power to the TTD lines. Within this enhanced bandwidth, the TTD lines maintain a phase error-free distribution across the RA aperture, ensuring optimal performance. Thus, the overall RA system demonstrates enhanced bandwidth performance analogous to its unit element.

To validate our proposed methodology, in what follows, we design an example RA based on it. More specifically, a traditional rectangular patch over ground plane is used as our antenna element. The dual connection points are realized with two appropriately placed conductive vias. The power combining network consists of a microstrip line that is placed behind the ground plane of the patch and connects the two points. Finally, a multi-meandered microstrip line is connected in series with the power combining microstrip line to achieve phase tuning of the different RA elements. This line operates as a true-time-delay line to induce the correct phase distribution with minimal phase errors across the increased frequency range. Notably, this is the first time that the FPT is used to increase the bandwidth of an antenna array.

III. DESIGN METHODOLOGY EXAMPLE: UNIT CELL

Utilizing our proposed methodology, we design a unit cell based on dual-fed patch elements. The geometry of our proposed dual-fed UC is shown in Fig. 2 along with the standard single-fed UC for comparison. The traditional single-fed UC consists of a patch antenna fed by a single probe (e.g., a metallized via). The probe is placed at the appropriate position along the length of the patch, as shown in Fig. 2, for realizing a 50 Ω input impedance. To introduce the desired phase shift variation, a 50 Ω microstrip line is employed behind the ground plane of the patch. Notably, a slot is etched at the ground plane of the patch to allow the connection of the probe with the microstrip line. Also, a conductive plate is placed behind the microstrip line to shield our design and suppress any spurious radiation. The materials used for the patch and line substrates are the Rogers RT/Duroid 5880 ($\epsilon_r = 2.2$, $tan\delta = 0.0009$) and Rogers

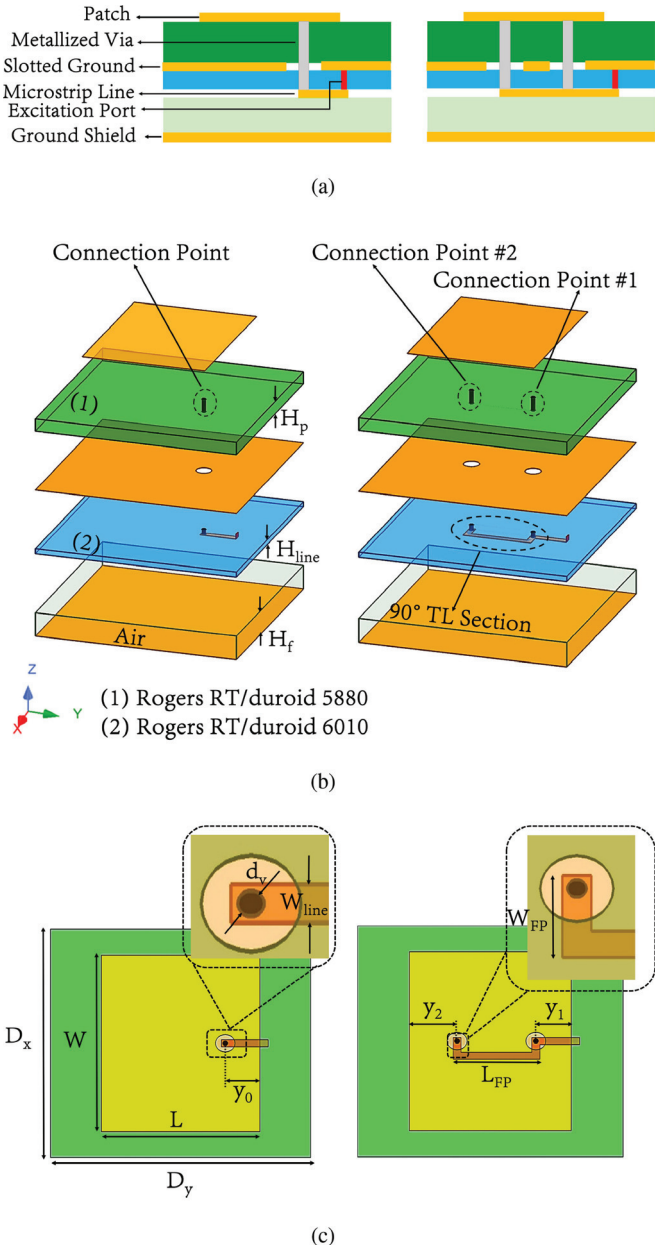

FIGURE 2. Single-fed (left figures) and dual-fed (right figures) UC in (a) side-, (b) exploded-, and (c) top-view (important design dimensions in mm: $D_x = D_y = 15$, $W = 11.59$, $L = 9.15$, $L_{FP} = 4.9$, $W_{FP} = 1.4$ $H_p = 1.575$, $H_{line} = 0.635$, $H_f = 6.35$, $W_{line} = 0.45$, $y_0 = 0.5$, $y_1 = 2$, $y_2 = 2.7$, $d_v = 0.3$).

RT/Duroid 6010 ($\epsilon_r = 10.2$, $tan\delta = 0.0023$) respectively (see Fig. 2).

Our proposed dual-fed UC is designed similarly to its traditional single-fed counterpart with the following key differences. First, two connection points are chosen to excite the patch according to the FPT design methodology. Both points are connected via their probes and through their corresponding slots to a properly designed 50 Ω microstrip line network placed behind the ground plane of the patch. Namely, the microstrip line network consists of a 90° TL section, placed between the two connection points, operating as the power combiner of Fig. 1(a). Notably, this structure

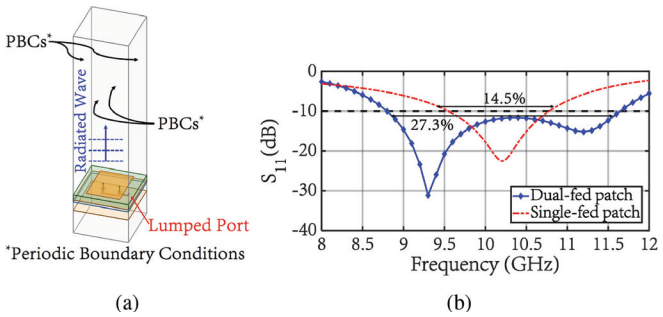

FIGURE 3. Simulation setup for lumped port evaluation, and (b) reflection coefficient versus frequency for the single- and dual-fed patch UCs.

is equivalent to a 2^{nd}-order filter according to the FPT [27]. Thus, our proposed dual-fed UC is expected to approximately double the bandwidth of the compared single-fed design [33]. Moreover, to introduce the desired phase shift variation, the microstrip line is properly extended beyond the first connection point as shown in Fig. 2. The dimensions of our design are included in Fig. 2.

A. LUMPED PORT EVALUATION

To verify the effectiveness of our design, we simulate both UCs of Fig. 2 under periodic boundary conditions and lumped port excitation. The simulation setup is shown in Fig. 3(a), and the corresponding reflection coefficient (S_{11}), measured at the lumped port, is plotted versus frequency in Fig. 3(b) for both UCs. Notably, our proposed dual-fed UC achieves a −10 dB bandwidth of 27.3% (from 8.85 GHz to 11.65 GHz), which is almost two times larger than the 14.5% bandwidth of the traditional single-fed UC.

B. FLOQUET PORT EVALUATION

The next step is to expand our proposed UC design to introduce the required phase variations needed by an RA aperture to collimate its beam towards a specific direction. To achieve this and provide the necessary phase in each of the RA elements, we extend the microstrip line beyond the first connection point of our UC as discussed previously. Notably, to accommodate the different lengths of lines into the limited space of our UC, we properly meander their lengths. To evaluate the reflective properties of our UC for different lengths of the meandered delay line, periodic boundary conditions are utilized in combination with an incident plane wave excited by a Floquet Port. Fig. 4(a) shows the employed simulation setup and the multi-meandered delay line utilized in our UC. Our proposed UC is simulated on ANSYS HFSS. Both the phase and amplitude responses are investigated as we vary the length, W_5 (see Fig. 4(a)), of the line and for three different frequencies of operation (e.g., 9 GHz, 10.25 GHz, and 11.5 GHz, that correspond to the lowest, middle, and highest frequency of operation of our UC). Fig. 4(b) shows the phase responses of the reflected wave and compares them to the perfectly linear response [the perfectly linear phase response is evaluated as $-2\beta(f)L$,

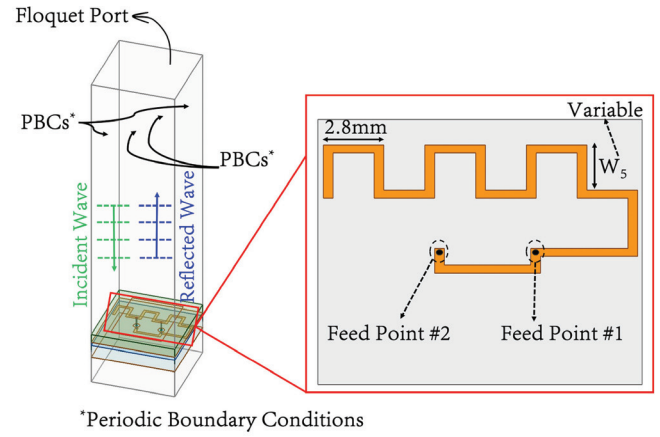

(a)

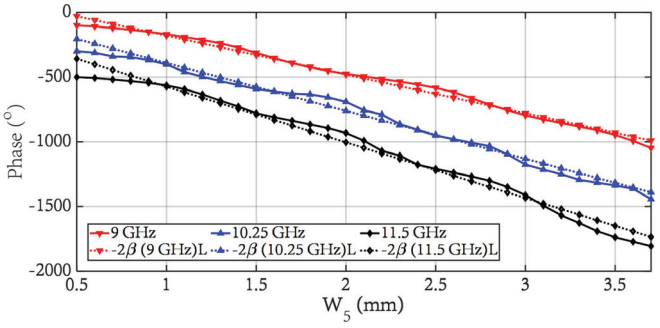

(b)

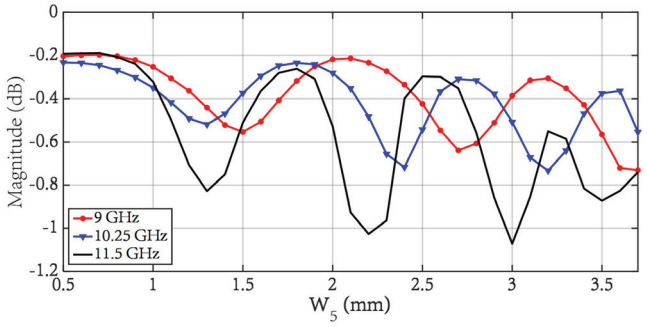

(c)

FIGURE 4. (a) Simulation setup for Floquet port evaluation and multi-meandered delay line network. The length W_5 is varied to achieve different phases. (b) Phase response of the reflected wave against the variable length of the multi-meandered delay line. (c) Magnitude response of the reflected wave against the variable length of the multi-meandered delay line.

where $\beta(f)$ is the propagation constant along the line at a frequency f, calculated as $\beta = 2\pi f\sqrt{\mu\epsilon}$; μ, ϵ correspond to the permeability and permittivity of the TTD line substrate, and L is the length of the line]. As it can be seen, the phase response is very close to the ideal linear response throughout the entire frequency band, thereby confirming the wideband operation of our UC. Also, Fig. 4(c) shows the magnitude response of the reflected wave for all the above cases. As it can be observed, our UC is highly reflective with a maximum reflection loss of 1.1 dB across all cases. Some resonances that appear, in the form of a dip in the magnitude (see Fig. 4(c)) and non-linearity in the phase (see Fig. 4(b)) of the reflected wave, are attributed to the fact that the TLs are resonant at specific lengths [22]. As a result, some of the energy from the Floquet port will be either stored in the form of standing waves along the TL or radiated as a spurious back lobe. In Fig. 4(c), it can also be seen that the losses increase with the length of the delay line or the frequency of operation. This is expected and it is attributed to the increase of the electrical length of the delay line (higher attenuation loss) and the increase of the electrical thickness of the line substrate, which results in undesired energy radiated towards the back direction.

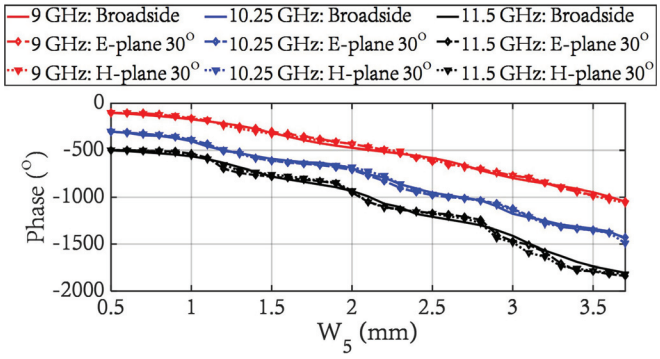

FIGURE 5. Phase response of our unit cell against the variable length W_5 of its delay line at 9 GHz, 10.25 GHz, and 11.5 GHz for incident angles of 30° at the E- and H- plane as well as broadside.

Finally, we simulate our proposed UC under different incident angles to demonstrate its performance for offset-feed, offset-beam configurations (i.e., when the EM wave is received from an angle away from broadside and it is focused in the specular quadrant). Specifically, Fig. 5 shows the phase response of our unit cell against the variable length W_5 of its delay line at 9 GHz, 10.25 GHz, and 11.5 GHz for the incident angles of 30^o at the E-, and H-plane as well as broadside. We observe that the phase response of our UC is stable with the variation of the incident angle. Similar responses are obtained at different frequencies inside the operational band (8.85 GHz to 11.65 GHz). However, these results are not shown for the sake of brevity. Therefore, our proposed UC is suitable for the design of wideband RAs with various offset angles of the feed and beam directions.

IV. DESIGN METHODOLOGY EXAMPLE: REFLECTARRAY

To validate our proposed methodology, we design a complete RA system utilizing the UC design presented in Section III. The design of an RA can be done in three steps: (1) specify the RA configuration, including aperture shape, number of elements, feed antenna type, position, and orientation, (2) compute the necessary phase distribution across the aperture to direct the beam as intended at the desired frequency, and (3) design each RA element to achieve the above-computed phase distribution.

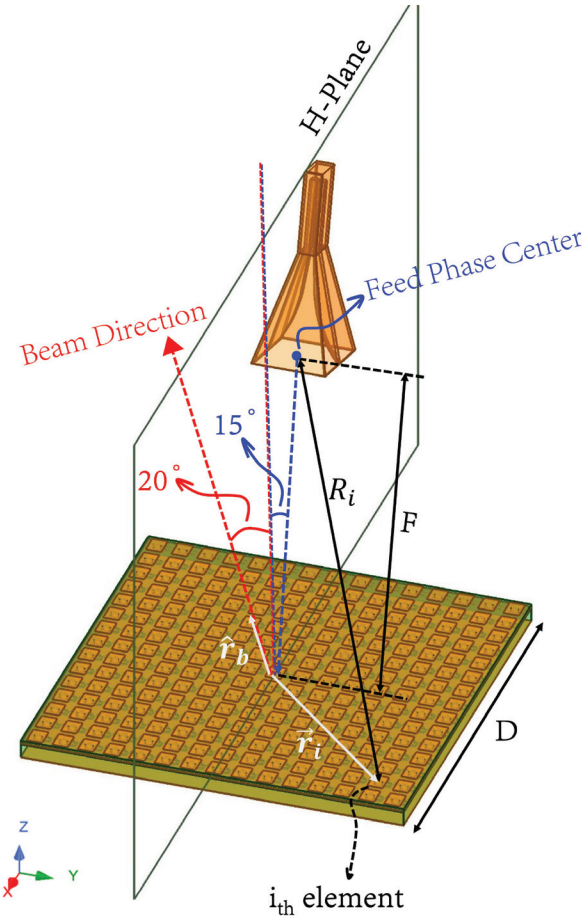

FIGURE 6. Geometry of our proposed reflectarray.

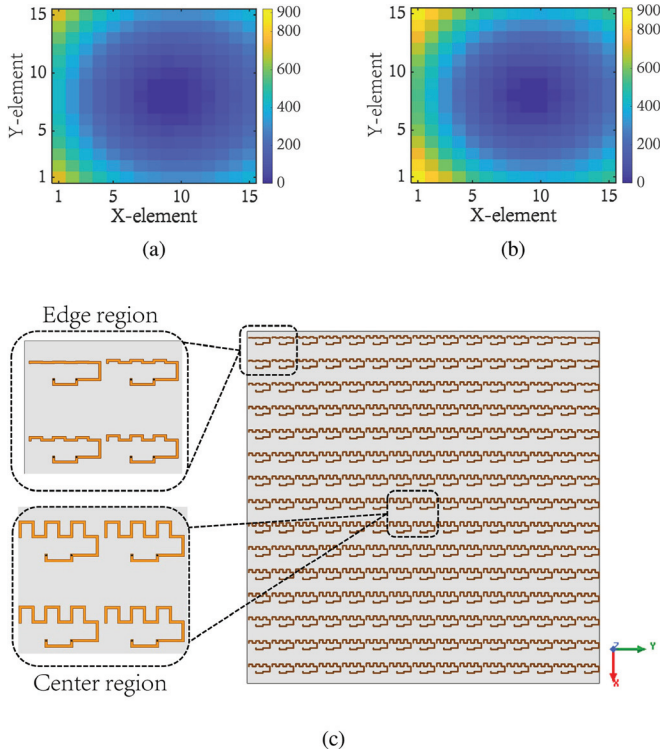

FIGURE 7. Unwrapped required phase distribution along the aperture at (a) 9 GHz, and (b) 11.5 GHz calculated using (1), and (c) delay line layer of the entire 15×15 RA.

A. RA APERTURE

Using our novel UC as a building block, we design the 15 × 15 RA shown in Fig. 6. The RA is fed by a single-polarized ridged horn antenna (A-Info LB-60180). To minimize the effect of feed blockage, an offset-feed, offset-beam configuration is chosen. Specifically, the feed is offset by −15° at the H-plane, while the beam is steered at +20° also at the H-plane. The total size of the RA is 225mm × 225mm and the focal length to aperture size ratio (commonly referred to as F/D ratio) is chosen to be approximately 0.83 for maximum aperture efficiency (at the center frequency of 10.25 GHz) as a compromise between illumination and spillover efficiency [2], [3].

B. RA SYNTHESIS METHOD

To collimate the RA beam in the specified direction, we tune the delay lines across the RA aperture to compensate the required phase distribution. More specifically, each UC needs to (a) compensate the spatial phase delay, which is the phase that the EM wave acquires when propagating from the feed phase center to each UC, and (b) add the progressive phase calculated by traditional array theory [2], [3]. Accordingly, the required ideal phase for the i^{th} UC is given by:

$$\phi_i^{req} = k_0(f)\left(R_i - \vec{r}_i \cdot \hat{r}_b\right) + \phi_{ref} = k_0(f)R_i^{total} + \phi_{ref}, \quad (1)$$

where $k_0(f)$ is the free-space propagation constant at frequency f, R_i is the distance between the feed phase center and the i^{th} UC, $\vec{r}_i$ is the position vector of the i^{th} UC, $\hat{r}_b$ is the unit vector of the main beam direction, and ϕ_{ref} is an arbitrary reference phase added to every UC. All geometric parameters are shown in Fig. 6.

The required ideal phase is plotted in Figs. 7(a), 7(b) along the RA aperture at the lowest and highest frequency inside our frequency band (i.e., 9 GHz and 11.5 GHz), respectively in its unwrapped form (extending to multiple cycles of 2π). For wideband RA operation, we tune the delay lines of each UC to compensate the unwrapped phase distribution. Specifically, we calculate the length of the delay line of each UC, so that the UC realized phase (see Fig. 4(b)) is equal to the required unwrapped phase (e.g., see Figs. 7(a), 7(b)) at the design frequency f. Consequently, the slope of the relative phase-frequency response between any two unit cells on the aperture [i.e., $-2\beta(f)(L_i - L_j)$; where L_i, L_j is the total length of the delay line of the i^{th}, j^{th} UC, respectively] is matched to that of the required phase $k_0(f)(R_i^{total} - R_j^{total})$, resulting in minimal phase error between them, across the entire frequency range. Notably, this synthesis method is insensitive to frequency, however, it is usually applied at the lowest operational frequency of a design, where the phase response is the most linear [23]. Therefore, we synthesize our delay lines at the lowest frequency of operation which in our case is at 9 GHz. Fig. 7(c) shows the corresponding delay lines.

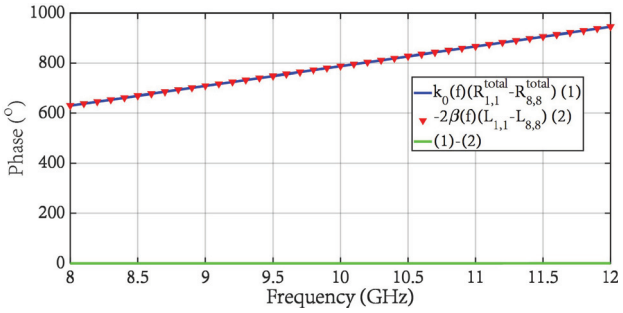

FIGURE 8. Ideal relative phase $k_0(f)(R_{1,1}^{total} - R_{8,8}^{total})$ and relative phase produced by the TTD lines $-2\beta(f)(L_{1,1} - L_{8,8})$ between the center (8, 8) and edge (1, 1) element.

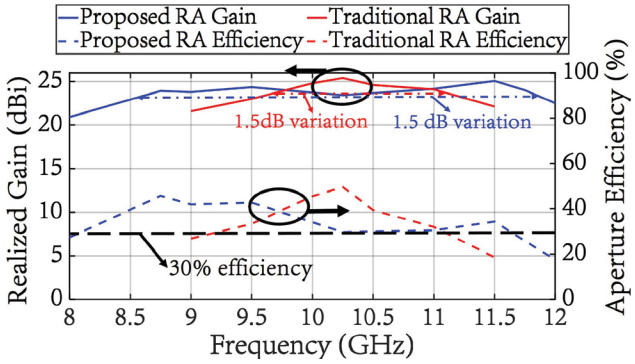

FIGURE 9. Realized gain of proposed and traditional RA based on dual- and single-fed patches respectively (aperture efficiency of both RAs is also included).

To showcase the performance of our phase compensation scheme, we present an example. Namely, we apply phase correction at a low frequency inside the band of interest (9 GHz) to calculate the lengths of the TTD lines along the aperture. The goal is to ensure that the relative phase introduced by the lines at 9 GHz, given by $-2\beta(9GHz)(L_i - L_j)$, aligns with the ideal relative phase between the same elements at 9 GHz, expressed as $k_0(9\ GHz)(R_i^{total} - R_j^{total})$. Consequently, we examine the phase correction for the relative phase between the center (8, 8) element and the edge (1, 1) element. For the center element, we have an equivalent delay of $R_{8,8}^{total} = 186$mm, while for the edge element, we have an equivalent delay of $R_{1,1}^{total} = 251.6$mm. To apply our phase correction at 9 GHz, we choose the length of the TTD lines for the center (8, 8) element and the edge (1, 1) element to satisfy the phase correction equation: $-2\beta(9\,GHz)(L_{1,1} - L_{8,8}) = k_0(9\ GHz)(R_{1,1}^{total} - R_{8,8}^{total})$, resulting in lines with lengths $L_{1,1} = 0$mm, $L_{8,8} = 10.3$mm. For these values, we plot the ideal and realized (by the lines) relative phase (versus frequency) between the center (8, 8) and the edge (1, 1) element in Fig. 8. We observe that our phase correction scheme results in no phase error independently of the frequency of operation even though it was applied at a single frequency, which is attributed to the TTD property of our design. Notably, our UC phase curves that are used for phase correction demonstrate slight deviations around the corresponding perfectly linear responses (see Fig. 4(b)), indicating that some slight phase errors can occur at frequencies different than the frequency where phase correction is applied.

V. REFLECTARRAY SIMULATION RESULTS

Our proposed RA is simulated in ANSYS HFSS to evaluate its radiation characteristics and validate the performance of our design method. Notably, to demonstrate the bandwidth increase achieved by our proposed methodology, we simulate both a traditional single-fed and our proposed dual-fed patch-based RA. The resulting realized gain in the direction of the main beam and the aperture efficiency are plotted versus frequency in Fig. 9 for both cases. The aperture efficiency is calculated by normalizing the realized gain to the maximum theoretical directivity given by the following equation:

$$D = 4\pi \frac{A}{\lambda^2} cos\theta, \tag{2}$$

where A is the physical aperture of the RA, λ is the free-space wavelength at the frequency of operation, and θ is the scan angle of the beam. To compare the performance of the two cases, we define the gain bandwidth as the frequency range where the gain results in an 1.5 dB variation from its maximum. As it can be seen from Fig. 9, our proposed RA achieves a fractional 1.5 dB gain bandwidth of 31% (from 8.6 GHz to 11.8 GHz), which is more than two times greater than the 14% bandwidth (from 9.7 GHz to 11.15 GHz) associated with the traditional RA with single-fed elements. However, we observe that, at the center frequency of 10.25 GHz, the traditional RA has almost 2 dB higher gain (corresponding to 20% higher aperture efficiency) than our proposed RA. This is attributed to the matching performance of the dual-fed patch compared to the single-fed one at this frequency. Specifically, the single-fed patch has its lowest S_{11} at 10.25 GHz, namely -23 dB, which corresponds to 0.02 dB of mismatch loss, while the dual-fed patch has its highest in-band S_{11}, namely -10 dB, which corresponds to a mismatch loss of 0.45 dB. Additionally, the dual-fed element exhibits lower gain at this frequency due to one more factor associated with its feeding scheme. Notably, the two connection points excite the same mode along the patch (i.e., the dominant TM_{010} mode), since they are placed along the length of the patch, but with a phase difference due to the line section between them (see Fig. 2). As a result, the radiated fields associated with the two modes partially cancel out leading to reduced gain (see Appendix A). This is an essential reason for the lower gain of the RA with dual-fed elements compared to the traditional design with single-fed elements. Both factors of mismatch loss and out-of-phase excitation are incorporated in the realized gain of both patch elements. For this purpose, we compare in Fig. 10 the realized gain of both the dual- and single-fed patches at 10.25 GHz (only the H-plane is shown which is the plane where each RA element receives the EM wave from the horn and re-radiates it after applying the appropriate phase). As

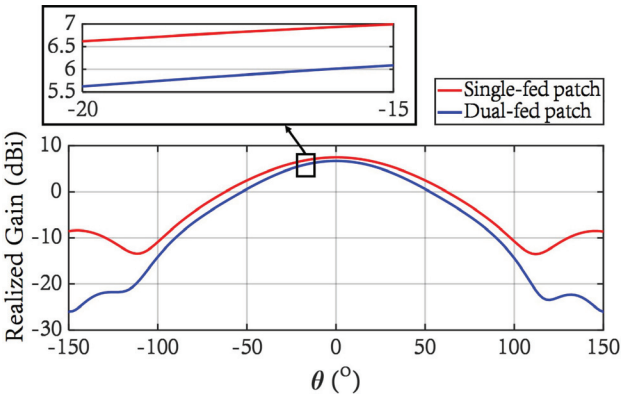

FIGURE 10. Realized gain pattern of dual- and single-fed patch at the H-plane. The inset shows patterns at the angles of reception (15°) and re-radiation (20°).

it can be seen, the dual-fed patch has indeed lower realized gain by approximately 1 dB compared to the single-fed patch. This gain reduction by 1 dB is applied twice (one for the reception and one for the re-radiation of the EM wave), resulting in the 2 dB gain difference between our proposed RA with dual-fed elements and the traditional RA with single-fed elements at 10.25 GHz (see Fig. 9).

Nonetheless, as it can be seen from Fig. 9, the aperture efficiency of the conventional RA with single-fed elements drops for frequencies that deviate around the center frequency of 10.25 GHz due to the narrowband matching of the single-fed patch (see Fig. 3(b)), while the aperture efficiency of our proposed RA with dual-fed elements has a stable response and is preserved at high values (greater than 30%) within its enhanced bandwidth (8.6 GHz to 11.8 GHz) due to the use of the FPT and TTD lines. More specifically, it is approximately 40% at the low end of our frequency band (8.6 GHz to 9.75 GHz), while it drops around 30% at the high end of our frequency band (10 GHz to 11.5 GHz). This drop in efficiency is attributed to the fact that our UC is lossier at higher frequencies, because of its long delay lines as explained in Section III and shown in Fig. 4(c). Notably, the aperture efficiency can be further increased according to the following observation. The gain of the available feed horn (A-Info LB-60180), that was used for the design of our proposed RA, has an average value of approximately 13 dBi in the frequency band of interest (from 9 GHz to 11.5 GHz). However, it is known from RA theory [3] that directive feeds with a minimum gain of 15 dBi are required to achieve maximum aperture efficiency. Thus, designing our proposed RA with an optimal feed will further improve the aperture efficiency.

Next, we examine the Co- and X-polarized radiation patterns of our proposed RA based on dual-fed patches at the E-[3] and H-plane and at multiple frequencies inside the frequency band of interest (namely, at 9 GHz, 10.25 GHz, and 11.5 GHz). The corresponding plots are shown in Fig. 11 from which we deduct the following:

[3]To extract the E-plane (normal to the plane of scanning) patterns, we rotate the global xyz-coordinate system shown in Fig. 6 around its y-axis, so that the new z-axis is aligned with the main beam direction.

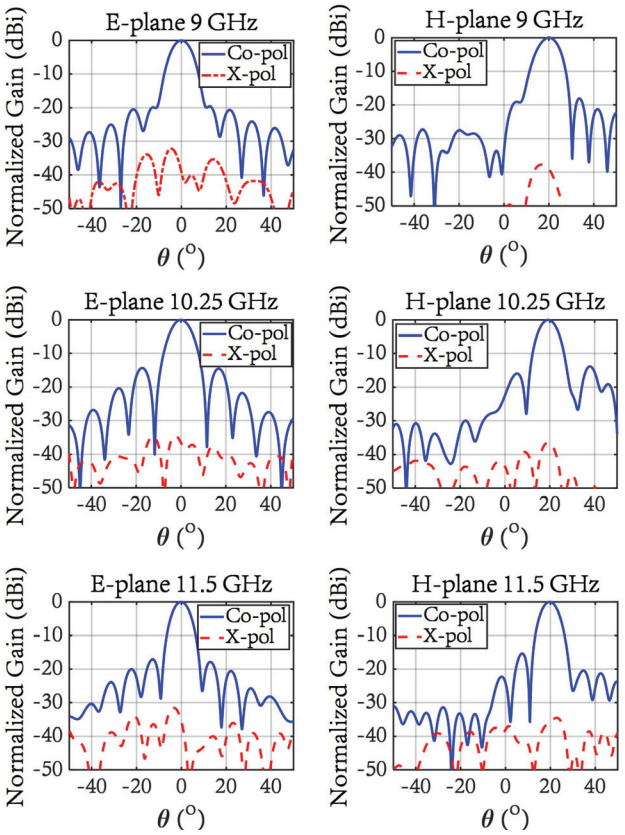

FIGURE 11. Normalized radiation patterns of the Co- and X-polarized gain at 9 GHz, 10.25 GHz, and 11.5 GHz.

1) The RA pattern is symmetric at the E-plane and asymmetric at the H-plane. This is attributed to the fact that the feed horn is placed at the H-plane with an offset angle of −15°, thereby, disrupting the symmetry of the entire system at this plane.
2) Our proposed RA exhibits great beam-pointing performance with minimal to zero beam squint across the entire frequency range. This is attributed to the employed TTD lines that produce the required phase distribution along the aperture with minimal to no phase errors across the entire bandwidth. The only case, where the beam squint is slightly noticeable, is for the H-plane pattern at 10.25 GHz. This slight beam squint (less than 1^o) is attributed to phase errors caused by the non-linearities in the phase response of the UC at 10.25 GHz (Fig. 4(b)) as well as to the slightly degraded matching between the patch and the delay line at 10.25 GHz (Fig. 3(b)), leading to EM power being reflected without the appropriate phase.
3) The side lobe level (SLL) of the E-plane pattern is around −20 dB for all the frequencies of Fig. 11 except for the pattern at 10.25 GHz that has an SLL of approximately −15 dB. Similarly, the SLL of the H-plane pattern is within the range of −16 dB to −19 dB

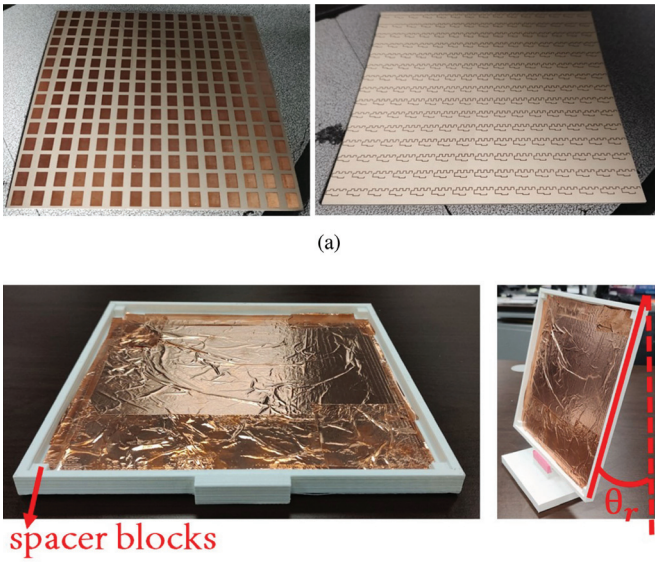

FIGURE 12. (a) Fabricated prototype of our proposed 15 × 15 RA. (b) 3D-printed support structure.

FIGURE 13. Setup for the measurement of our proposed RA in the MVG StarLab.

for all the frequencies of Fig. 11 except for the pattern at 10.25 GHz that has an SLL of approximately −14 dB. The increased SLL of both E- and H-plane patterns at 10.25 GHz is also attributed to the phase errors caused by the non-linear phase response as well as the degraded matching between the patch elements and the corresponding delay lines at 10.25 GHz as explained above.

4) Our proposed RA demonstrates high polarization purity with X- to Co-pol ratio below −30 dB within the main beam solid angle for the entire frequency range.

The wide bandwidth, high aperture efficiency, radiation pattern with good beam formation, low SLL, and low X-pol level have also been verified for RA examples with larger apertures (i.e., a 30 × 30 element RA corresponding to 15λ × 15λ at the center frequency of 10.25 GHz) and for various angles of incidence and beam-scanning (i.e., feed placed at −25° and beam scanned to +30°). These results and their detailed analysis are included in Appendix B.

VI. FABRICATION AND SIMULATION ADJUSTMENT

Our proposed RA was fabricated using standard printed circuit board (PCB) technology and it is shown in Fig. 12(a). On the left of Fig. 12(a), the top layer comprised of the patch radiators is shown, while on its right, the bottom layer comprised of our delay microstrip lines is shown. To realize the correct setup for the measurement of our RA, we fabricated a support structure using our 3D printers. The support structure is shown in Fig. 12(b) and has two key features for the successful setup of the measurement, namely (a) the design of square spacer blocks at its four edges in order to hold the RA at the right distance above its back side which is covered with copper tape to implement the metallic shield back plate (see Fig. 12(b), left picture) and (b) the design of the RA holding part to have the right tilt angle $\theta_r = 15^o$ for achieving the offset-feed offset-beam configuration that we used in the simulation (see Fig. 12(b), right picture).

Notably, there are two critical factors that differentiate the fabricated RA and measurement setup from the initial simulated RA and setup; namely, (a) the support structure resulted in a tilting angle θ_r (see Fig. 12(b), right picture) equal to 20^o instead of the 15^o of the initial simulation model, and (b) the material used for the delay lines substrate (RT/duroid 6010.2LM with $\epsilon_r = 10.2 \pm 0.25$) was characterized and its dielectric constant was found to be approximately 10.8 instead of 10.2, as it was in the initial simulation setup. Taking these two key factors into account, we adjust our simulation setup (feed offset of -20^o instead of the initial -15^o and delay line substrate of $\epsilon_r = 10.8$ instead of the initial $\epsilon_r = 10.2$) to match the setup of the measurement and simulate our proposed RA again. Notably, in this adjusted simulation, the RA delay line layer is the same as the one shown in Fig. 7(c) that was calculated with the initial setup parameters (i.e., feed offset of -15^o and delay line substrate of $\epsilon_r = 10.2$). In this manner, we ensure a fair comparison between the adjusted simulation's and measurement's results as shown in the next section.

VII. MEASUREMENT AND VALIDATION

Utilizing our 3D-printed support structure, the proposed RA was measured using our MVG StarLab near-field anechoic chamber. Fig. 13 shows our measurement setup.

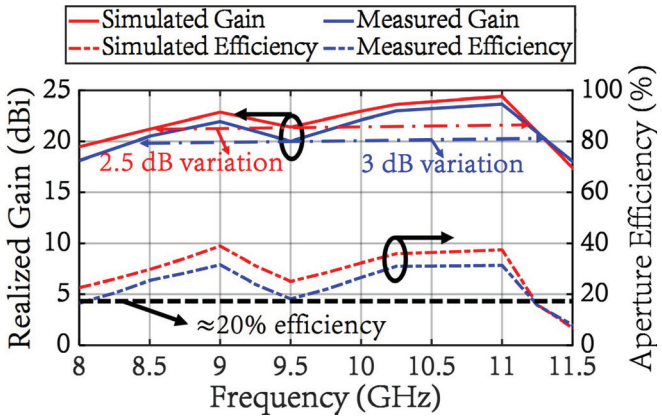

FIGURE 14. Measured and simulated realized gain (and aperture efficiency) vs frequency.

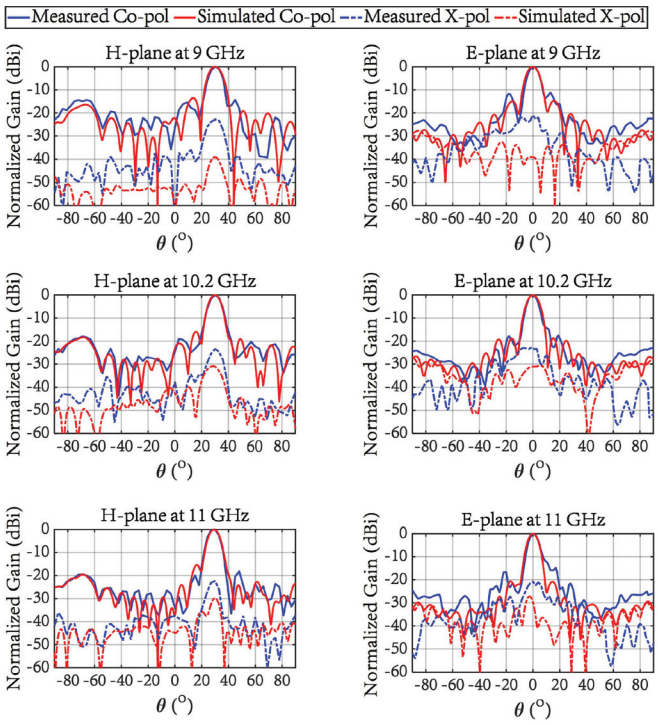

FIGURE 15. Measured and simulated normalized patterns at 9 GHz, 10.2 GHz, and 11 GHz (E- and H-plane patterns for both the Co- and X-pol components).

In Fig. 14, the simulated (corresponding to the adjusted setup) and measured realized gain and aperture efficiency at the main beam direction are presented. Notably, there is excellent agreement between simulated and measured results. We observe that the measured gain and aperture efficiency are approximately 1 dB and 10% lower than the simulated ones, respectively. This is attributed to misalignment and misplacement errors during our measurements, as RA measurements can be quite sensitive to such errors, in addition to fabrication errors [23]. Specifically, the simulation results of our proposed RA (red curves in Fig. 14) demonstrate a 2.5 dB gain bandwidth of 26% (from 8.6 GHz to 11.2 GHz) with a minimum aperture efficiency of 25%, while the measured results (blue curves in Fig. 14) demonstrate a 3 dB gain bandwidth of 29% from 8.4 GHz to 11.25 GHz with a minimum aperture efficiency of approximately 20%. The simulated and measured maximum aperture efficiency is 45% and 35%, respectively.

Next, the measured Co- and X-pol normalized patterns at 9 GHz, 10.2 GHz, and 11 GHz and for both the E- and H-plane cuts are shown in Fig. 15 along with the corresponding simulation data. As it can be seen, excellent agreement is observed between simulations and measurements across all cases in terms of general pattern form and beamwidth. Moreover, both measured and simulated patterns demonstrate great beam-pointing performance across the entire operational bandwidth, as is expected due to the use of TTD lines. The slight discrepancies observed in X-pol levels and SLL are attributed to the measurement setup. The measured X-pol levels are higher than the simulated ones within the main beam, likely due to scattering and reflections from the 3D-printed support structure, the horn, and the feeding cable (see Fig. 13). While the simulated X- to Co-pol ratio is below −30 dB, the measured ratio is below −20 dB. Additionally, the measured patterns show increased SLL, particularly in the E-plane, due to these scattered components and potential phase errors from misalignment or fabrication issues. The maximum measured SLL is −12 dB at 9 GHz, with other measurements ranging from −15 dB to −20 dB.

VIII. DISCUSSION AND COMPARISON

Our simulated and measured results showed good agreement in terms of realized gain, aperture efficiency, and pattern formation, thus, validating our design method.

To emphasize the advantages of our proposed design methodology, we compare our example RA to other reported wideband RAs in Table 1. Notably, all the designs in Table 1 are of planar structure for a fair comparison. Additionally, a key metric is introduced to compare the fabrication complexity across all designs. Specifically, we define design complexity based on the scalability of each design to higher frequencies while adhering to the minimum achievable tolerances of the fabrication method employed. For this comparison, we consider the capabilities and limitations of the PCB manufacturing process. The fabrication complexity of a PCB-based design is limited by a number of different factors, such as via spacing, trace width, and copper trace spacing (or slot size), which indicates the need of a complexity metric that can account for these factors. To enable a fair comparison, we introduce the Design Complexity Coefficient (DCF), defined as the ratio of a predefined maximum frequency F_M (arbitrarily set here to 100 GHz) to the maximum scalable frequency (F_{MSF}) that a given design can achieve. The formula is expressed as:

$$DCF = \frac{F_M}{F_{MSF}}, \tag{3}$$

TABLE 1. Comparison of our proposed RA with other wideband RAs in the literature.

Ref.	UC Type	UC Phase Range	Center Frequency	Aperture Size	Gain Bandwidth[¶,†]	RA Profile[*]	Aperture Efficiency[¶]	SLL[§]	X-pol level[§]	DCF[▮] / No. of Layers / No. of Vias per UC
[12]	Square ring	360^o	13.5 GHz	$18\lambda_0$	15.7%-1.5 dB (16.7%-1.5 dB)	$0.07\lambda_0$[‡]	54% (42%)	−9 dB	N/A	1.43 / 1 / 0
[14]	Ring patch with interior concave arm	330^o	10 GHz	$14.3\lambda_0$	29%-1 dB (29%-1 dB)	$0.106\lambda_0$	60% (66%)	−18.5 dB	−35.1 dB	7.59 / 1 / 0
[16]	Spiral dipole	330^o	8 GHz	$8\lambda_0$	29%-1 dB (35%-1 dB)	$0.053\lambda_0$	68% (64%)	−7 dB	−30 dB	1.88 / 1 / 0
[17]	Circular cosine curve element	330^o	5.8 GHz	$18.5\lambda_0$	17%-1 dB (20%-1 dB)	$0.17\lambda_0$	55% (52.9%)	−7.5 dB	−21 dB	12.5 / 2 / 0
[18]	Stacked patch	640^o	12 GHz	$16.25\lambda_0$	16.7%-1.5 dB (16.7%-1.5 dB)	$0.24\lambda_0$	52.5% (52.5%)	−18 dB	−25 dB	0.625 / 2 / 0
[22]	Aperture coupled patch	950^o	9.65 GHz	$26.5\lambda_0$	26.7%-1.5 dB[**]	$0.1\lambda_0$	67%[**]	−20 dB[**]	−30 dB[**]	0.77 / 3 / 0
This work	Probe-fed patch	950^o	10.25 GHz	$7.5\lambda_0$	31.5%-1.5 dB (29%-3 dB)	$0.07\lambda_0$	45% (35%)	−12 dB	−23 dB	1.65 / 2 / 2

[¶] In order to conduct a fair comparison, both simulated and measured results are included with the measured ones inside parenthesis.

[†] The fractional gain bandwidth is provided with the corresponding gain variation.

[*] RA profile is defined as the distance from top to bottom surface of the RA.

[§] Measured data are used.

[▮] Design Complexity Coefficient.

[‡] λ_0 is the free-space wavelength at the center frequency.

[**] The results mentioned in [22] correspond to analytical calculation of the total reflected fields by the RA, utilizing unit cell simulation data. This method is semi-analytical and does not take into account important practical factors, such as feed blockage, edge diffraction, etc. Thus, the bandwidth, aperture efficiency, SLL, and X-pol level of the RA in [22] are expected to be degraded in a realistic simulation and measurement configuration.

As it can be seen, the higher the maximum scalable frequency (F_{MSF}) is, the lower the design complexity coefficient DCF is. Therefore, designs with high complexity will exhibit a higher DCF compared to those with lower complexity. The design complexity coefficient that we use here may seem unconventional compared to other commonly used metrics, such as the number of layers or vias, which are also included in Table 1 for a complete comparison. However, we believe that it provides a more accurate measure of fabrication complexity, as it accounts for critical design features that determine whether a design can be successfully manufactured or not. When compared to other patch-based RAs, such as the stacked patch RA in [18] and the RA with aperture coupled patches to TTD lines in [22], our proposed RA results in greater bandwidth and decreased profile, while exhibiting similar aperture efficiency and increased fabrication complexity. When compared to RAs that use the variable size technique with complex patch shapes, such as the designs in [14], [16], and [17], our proposed RA demonstrates similar or greater bandwidth, similar profile, similar aperture efficiency, but much lower design complexity. The RAs in [14], [16], [17] are all single layer designs with no vias and might appear as low fabrication complexity designs at first glance. However, to achieve their demonstrated performance (e.g., wide bandwidth), they include copper traces positioned at distances that approach the limits of PCB manufacturing tolerances. This makes their fabrication extremely challenging, and highly prone to fabrication errors, even at low microwave frequencies, such as 10 GHz. For example, the unit cell design in [14] consists of two connected loops that appear simple to fabricate. However, if we look closer, we will see that the minimum distance between the two loops is $100\mu m$ (denoted as h_3 in [14]), which is very close to the PCB manufacturing tolerance of $76\mu m$ (see for example Fig. 2 in [34]). Therefore, the RA presented in [14], while seemingly straightforward to fabricate, becomes highly challenging to scale for operation at higher frequencies. To quantify this design complexity, we use the DCF, as discussed above. Calculating the DCF requires evaluating the maximum scalable frequency F_{MSF}. This can be determined by taking the ratio of the minimum critical dimension in the design to the corresponding PCB

fabrication tolerance. For the unit cell design in [14] this critical dimension is the distance between the copper traces. In this case, the ratio is calculated as $\frac{100}{76} = 1.3158$, indicating that the design can be scaled by a factor of approximately 1.32. Using the center frequency of operation for this design, the maximum scalable frequency is roughly 13.2 GHz. Thus, the resulting DCF is calculated as $\frac{100}{13.2} = 7.59$. If we now take our design, the minimum critical dimension corresponds to the trace width, which is $450\mu m$, compared to the minimum PCB-supported trace width of $76\mu m$. As a result, our design can be scaled by a factor of $\frac{450}{76} = 5.9211$, increasing its center frequency from 10.25 GHz to 60.69 GHz. This gives a *DCF* of $\frac{100}{60.6913} = 1.6477$. Similar improvements in complexity and scalability are observed when comparing our design with those in [16] and [17]. Moreover, our proposed RA demonstrates greater bandwidth, similar aperture efficiency, similar profile, and similar design complexity compared to the RA in [12], which utilizes the variable size technique in conjunction with optimization methods. It is also worth noting that our design has greater or equal UC phase range compared to all the designs in Table 1, demonstrating its ability to maintain its wideband performance for RA apertures of greater size for high-gain applications. Finally, our proposed RA is highly competitive in terms of SLL and X-pol level with all the other RAs in Table 1. Overall, utilizing our proposed design methodology, we demonstrated an example planar RA that outperforms all the planar RAs in Table 1 in terms of BW (except for the RA in [16] that has similar BW performance) without compromising its other characteristics, such as its low profile and high efficiency, but most importantly while exhibiting lower design complexity and improved frequency scalability.

An important point of discussion is the scalability of our proposed design method to use more connection points for further enhancement of the RA bandwidth. In theory, by utilizing the FPT methodology we can indeed increase the bandwidth of an antenna N times when N points are used. We have theoretically proved that in [33] and we have experimentally demonstrated it to some extent with patch antennas. Therefore, by extrapolation, the use of more than two connection points (i.e., $N > 2$ points) could be exploited in RA design to increase the bandwidth of the RA by N times. However, after a certain number of points, the radiation efficiency of the design is degraded inside the enhanced bandwidth. Our studies have shown thus far that the FPT can increase the bandwidth by 5 times (utilizing 5 points) without degrading the radiation efficiency. For a detailed analysis, we refer the interested reader to [33]. Finally, it can be noted that our design method can be extended to support circular polarization (CP) operation. This can be achieved by employing four points (two for the H-pol and two for the V-pol) connecting the patch to a carefully designed network consisting of power combiners to apply the FPT. Additionally, a wideband 90° phase shifter will need to be used to achieve CP, while a TTD line will be incorporated to introduce the necessary phase distributions for beam-forming.

IX. CONCLUSION

In this work, a new design method for wideband RAs was introduced. An example RA based on planar patch elements was designed utilizing our proposed methodology. Our designed RA demonstrated increased BW performance with high efficiency, low profile, and low complexity. This was made possible by increasing the bandwidth of each patch element using the frequency pulling technique (FPT) and employing true-time-delay (TTD) lines to provide the required phase distribution across the entire bandwidth with minimal phase errors. First, we designed a dual-fed patch UC with increased BW based on the FPT. Then, we expanded our UC design by including TTD meandered microstrip lines to achieve the required phase distributions along the RA aperture for effective beamforming. Utilizing our novel UC, we successfully designed an RA aperture. Finally, the enhanced bandwidth performance of our proposed RA was validated through simulations in ANSYS HFSS and measurements, which agreed very well. When compared to other planar wideband RAs in the literature, our proposed RA demonstrated greater or similar bandwidth, while preserving low profile, high efficiency, and most importantly low design complexity. It should be pointed out that our methodology can be applied to increase the bandwidth of most (if not all) existing RA designs that employ transmission lines of variable length for beamforming, i.e., [20], [21], [22], [23]. More precisely, according to our methodology, the bandwidth of such RAs is nearly doubled when dual-fed elements are utilized for the RA design, while it can be even further increased when elements with more connection points are used. Therefore, our work paves the way to the development of broadband high-gain antennas, such as reflectarray and transmittarray antennas.

APPENDIX A
MODE CANCELLATION AND RA GAIN REDUCTION ANALYSIS

To prove that the gain reduction of the RA with dual-fed elements compared to the traditional design with single-fed elements is due to the excitation of two out-of-phase modes we conduct the following study. First, we simulate our UC without the microstrip combining network. The model consists of the patch, its ground plane, the two feeding vias, and two wave-ports on the ground plane level (see Fig. 16(a)). We use this model to acquire the modal fields associated with each connection point. Notably, we simulate the model, and plot the induced currents on the patch assuming connection point 1 is excited while connection point 2 is match terminated and vice versa (see Figs. 16(b) and 16(c)). From Figs. 16(b) and 16(c) we can observe that the two connection points excite the same mode

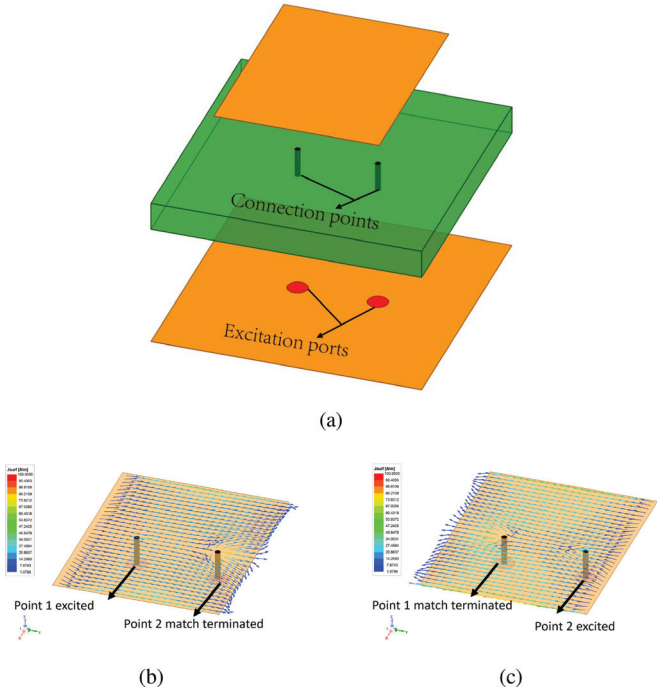

FIGURE 16. (a) UC without microstrip combining network (exploded view), and induced current on the patch when exciting (b) connection point 1 or (c) connection point 2.

along the patch (i.e., the dominant TM_{010} mode) with 180° phase difference (notice the opposite current direction in Figs. 16(b) and 16(c)) and a slight amplitude imbalance due to slightly asymmetric connection point positions.

To fully evaluate the effect of mode cancellation, we need to compute the phase difference that is introduced by the power combining microstrip network between the two connection points. Notably, the microstrip combining network consists of a microstrip line that connects the two points into one (see Fig. 17). This line is responsible for increasing the bandwidth of the unit cell. The power combining microstrip network is modeled, simulated, and it is found that it introduces a phase shift of 135° and a loss of −0.125 dB (0.985 in voltage ratio) at the center frequency of 10.25 GHz. Note that this is the frequency, where the proposed dual-fed element RA exhibits 2 dB lower gain than the gain of a traditional single-fed element RA as shown in Fig. 9.

As a result, the total phase difference between the modes is $180° + 135° = 315° = -45°$, causing partial cancellation of the radiated fields and gain reduction. To analytically estimate the gain reduction of the RA with dual-fed elements compared to the RA with single-fed elements, we do the following calculation. Let us assume that each connection point causes a radiated E-field of 1 V/m at an arbitrary observation angle. If both connection points were excited in phase, the total radiated E-field at the same observation angle would have been 2 V/m. However, when the patch is fed with the power combing network, the two connection points are excited with −45° of phase difference and a loss of

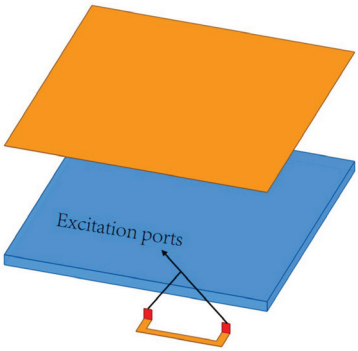

FIGURE 17. Power combining microstrip network (exploded view).

−0.125 dB (0.985 in voltage ratio) for one of the connection points, thus radiating an E-field at that observation angle equal to $|1 + 0.985e^{-j\pi/4}| = 1.83\ V/m$. In this case, the UC gain reduction due to this field cancellation can be easily computed as $20log(1.83/2) = -0.77$ dB. However, this reduction in the UC gain is applied twice in the case of an RA (receive and re-radiate), resulting in 1.54 dB of gain reduction, which is very close to the 2 dB gain difference between the proposed RA with dual-fed elements and the traditional RA with single-fed elements that our simulations predict (see Fig. 9).

APPENDIX B
GENERALIZATION OF PROPOSED DESIGN METHOD TO VARIOUS RA APERTURES

To validate that our method is agnostic to the size of the RA aperture, the angle of incidence from the horn, and the angle of beam-steering, we design the following apertures:

1) a 30 × 30 RA (15λ × 15λ at the center frequency of 10.25 GHz) based on our proposed unit cell, using the same RA setup as in the manuscript (i.e., the feed is placed with an offset angle of −15° and the beam is steered +20° in the specular direction). We will refer to this RA as RA_1,
2) a 30 × 30 RA (15λ × 15λ at the center frequency of 10.25 GHz), using an RA setup where its feed is placed with an offset angle of −25° and the RA's beam is steered at +30° in the specular direction. We will refer to this RA as RA_2.

For comparison purposes, we will refer to the 15 × 15 RA of the manuscript as RA_0.

The results of RA_1 are shown in Fig. 18 and Fig. 19. Specifically, the realized gain along with the corresponding aperture efficiency are shown in Fig. 18 and the E-, H-plane patterns at different frequencies across the operating band are shown in Fig. 19. We can observe from Fig. 18 that RA_1 exhibits wideband and high aperture efficiency characteristics similar to RA_0. More specifically, RA_1 has a 2.5 dB gain bandwidth of 28.5% (from 8.8 GHz to 11.7 GHz) with a minimum aperture efficiency of 25% and a maximum aperture efficiency of 45%, while RA_0 has a 1.5 dB gain bandwidth of 31% (from 8.6 GHz to 11.8 GHz) with a minimum aperture efficiency of 30% and a maximum aperture efficiency of

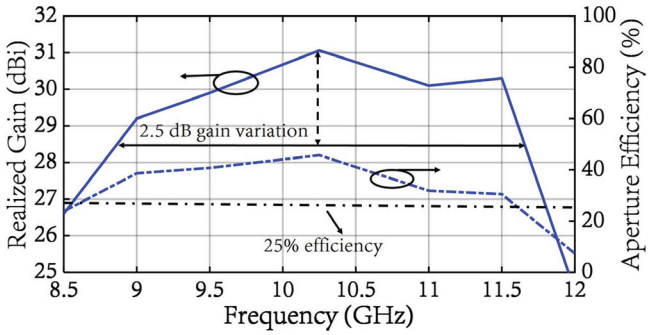

FIGURE 18. Realized gain and aperture efficiency of RA_1.

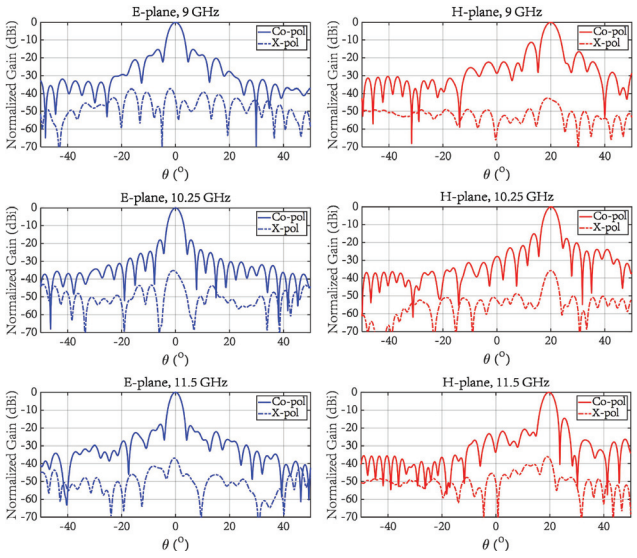

FIGURE 19. Normalized radiation patterns of RA_1 for the Co- and X-polarized gain at 9 GHz, 10.25 GHz, and 11.5 GHz.

45% (see Fig. 9). Notably, RA_1 has higher gain variation inside the operating bandwidth compared to RA_0, i.e., gain variation of 2.5 dB for RA_1 and 1.5 dB for RA_0, respectively. Also, RA_1 has lower minimum aperture efficiency compared to RA_0, i.e., aperture efficiency of 25% for RA_1 and 30% for RA_0, respectively. The degradations both in gain variation and aperture efficiency are attributed to the fact that RA_1 requires longer TTD lines to cover its increased phase range, thus increasing the line losses. Also, Fig. 19 demonstrates that RA_1 achieves advantageous pattern characteristics, i.e., low SLL (−15 dB on average), low X- to Co-pol ratio (−35 dB on average), and great beam-pointing with minimal to no beam squint, similarly to RA_0. Finally, we can observe that increasing the RA size from $7.5\lambda \times 7.5\lambda$ (RA_0) to $15\lambda \times 15\lambda$ (RA_1) results in similar gain bandwidth (31% for RA_0 and 28.5% for RA_1) but with increased gain variation (1.5 dB for RA_0 versus 2.5 dB for RA_1). This is effectively equivalent to a reduction in gain bandwidth while maintaining similar gain variation. Notably, comparable trends are observed in other electrically large reflectarray designs reported in the literature, such as in [22], which demonstrated a fractional

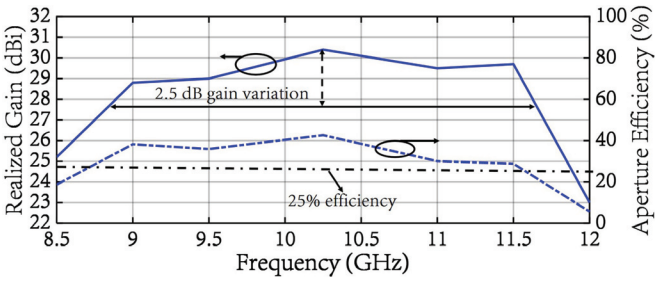

FIGURE 20. Realized gain and aperture efficiency of RA_2.

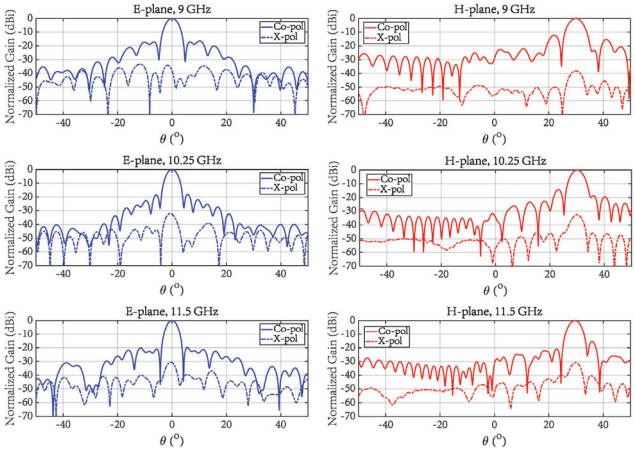

FIGURE 21. Normalized radiation patterns of RA_2 for the Co- and X-polarized gain at 9 GHz, 10.25 GHz, and 11.5 GHz.

bandwidth of 26.7% with a gain variation of 1.5 dB for a 26.5λ diameter-long circular RA aperture.

The results of the 30 × 30 RA with wider incident and beam-steering angles (RA_2) are shown in Fig. 20 and Fig. 21. Notably, RA_2 demonstrates wide bandwidth (2.5 dB gain bandwidth of 28.5% from 8.8 GHz to 11.7 GHz, see Fig. 20), high aperture efficiency inside the operating bandwidth (minimum aperture efficiency of 25% and maximum aperture efficiency of 42%, see Fig. 20), and advantageous pattern characteristics (average SLL of −15 dB, average X- to Co-pol ratio of −35 dB, minimal to no beam-squint, see Fig. 21), similarly to RA_1 and RA_0. These results validate our design method for incident and beam-steering angles within a scan cone of 60°. Using [32], we have calculated that our UC achieves grating-lobe free scanning roughly within a scan cone of 90° for its entire operating bandwidth. Thus, it can be extrapolated that our design method can increase the bandwidth for angles of incidence and beam-steering up to ±45°, even though it still needs to be experimentally verified for angles wider than ±30°. However, RAs are traditionally used in high distance links due to their high gain. Consequently, scanning within a cone of 60° is deemed sufficient for most applications.

REFERENCES

[1] D. Berry, R. Malech, and W. Kennedy, "The reflectarray antenna," *IEEE Trans. Antennas Propag.*, vol. 11, no. 6, pp. 645–651, Nov. 1963.

[2] J. Huang and J. A. Encinar, *Reflectarray Antennas*. Hoboken, NJ, USA: Wiley, Mar. 2007. [Online]. Available: http://dx.doi.org/10.1002/9780470178775

[3] P. Nayeri, F. Yang, and A. Z. Elsherbeni, *Reflectarray Antennas: Theory, Designs, and Applications*. Hoboken, NJ, USA: Wiley, Feb. 2018. [Online]. Available: http://dx.doi.org/10.1002/9781118846728

[4] J. Huang and R. Pogorzelski, "A ka-band microstrip reflectarray with elements having variable rotation angles," *IEEE Trans. Antennas Propag.*, vol. 46, no. 5, pp. 650–656, May 1998.

[5] S. Hum and M. Okoniewski, "An electronically tunable reflectarray using varactor diode-tuned elements," in *Proc. IEEE Antennas Propag. Soc. Symp.*, vol. 2, 2004, pp. 1827–1830.

[6] S. Montori et al., "A transportable reflectarray antenna for satellite ku-band emergency communications," *IEEE Trans. Antennas Propag.*, vol. 63, no. 4, pp. 1393–1407, Apr. 2015.

[7] D. Pozar, "Bandwidth of reflectarrays," *Electron. Lett.*, vol. 39, no. 21, p. 1490, 2003. [Online]. Available: http://dx.doi.org/10.1049/el:20030990

[8] J. Huang, "Bandwidth study of microstrip reflectarray and a novel phased reflectarray concept," in *Proc. IEEE Antennas Propag. Soc. Int. Symp. Dig.*, vol. 1, 1995, pp. 582–585.

[9] R. Javor, X.-D. Wu, and K. Chang, "Design and performance of a microstrip reflectarray antenna," *IEEE Trans. Antennas Propag.*, vol. 43, no. 9, pp. 932–939, Sep. 1995.

[10] E. Carrasco, J. A. Encinar, and M. Barba, "Wideband reflectarray antenna using true-time delay lines," in *Proc. 2nd Eur. Conf. Antennas Propag.*, 2007, pp. 1–6.

[11] D. Pozar and T. Metzler, "Analysis of a reflectarray antenna using microstrip patches of variable size," *Electron. Lett.*, vol. 29, no. 8, p. 657, 1993. [Online]. Available: http://dx.doi.org/10.1049/el:19930440

[12] Y. Mao, S. Xu, F. Yang, and A. Z. Elsherbeni, "A novel phase synthesis approach for wideband reflectarray design," *IEEE Trans. Antennas Propag.*, vol. 63, no. 9, pp. 4189–4193, Sep. 2015.

[13] Q.-Y. Chen, S.-W. Qu, X.-Q. Zhang, and M.-Y. Xia, "Low-profile wideband reflectarray by novel elements with linear phase response," *IEEE Antennas Wireless Propag. Lett.*, vol. 11, pp. 1545–1547, 2012.

[14] M. Guo, L. Guo, W. Feng, and X. Chen, "A single-layered broadband reflectarray employing 0.15-wavelength elements," *IEEE Antennas Wireless Propag. Lett.*, vol. 22, pp. 318–322, 2023.

[15] M. Min and L. Guo, "Design of a wideband single-layer reflectarray antenna using slotted rectangular patch with concave arms," *IEEE Access*, vol. 7, pp. 176197–176203, 2019.

[16] X. Li, X. Li, Y. Luo, G. Wei, and X. Yi, "A novel single layer wideband reflectarray design using two degrees of freedom elements," *IEEE Trans. Antennas Propag.*, vol. 69, no. 8, pp. 5095–5099, Aug. 2021.

[17] D. Su, H. Zhang, H. Xiao, W. Song, H. Xiong, and D. Xiao, "Broadband reflectarray using circular cosine curve elements," *IEEE Antennas Wireless Propag. Lett.*, vol. 22, pp. 238–242, 2023.

[18] J. A. Encinar, "Design of two-layer printed reflectarrays using patches of variable size," *IEEE Trans. Antennas Propag.*, vol. 49, no. 10, pp. 1403–1410, Oct. 2001.

[19] Y. Li, M. E. Bialkowski, and A. M. Abbosh, "Single layer reflectarray with circular rings and open-circuited stubs for wideband operation," *IEEE Trans. Antennas Propag.*, vol. 60, no. 9, pp. 4183–4189, Sep. 2012.

[20] D.-C. Chang and M.-C. Huang, "Multiple-polarization microstrip reflectarray antenna with high efficiency and low cross-polarization," *IEEE Trans. Antennas Propag.*, vol. 43, no. 8, pp. 829–834, Aug. 1995.

[21] E. Carrasco, M. Barba, and J. A. Encinar, "Reflectarray element based on aperture-coupled patches with slots and lines of variable length," *IEEE Trans. Antennas Propag.*, vol. 55, no. 3, pp. 820–825, Mar. 2007.

[22] E. Carrasco, J. A. Encinar, and M. Barba, "Bandwidth improvement in large reflectarrays by using true-time delay," *IEEE Trans. Antennas Propag.*, vol. 56, no. 8, pp. 2496–2503, Aug. 2008.

[23] M. Hamza, C. L. Zekios, and S. V. Georgakopoulos, "A low profile planar dual-polarized tightly coupled dipole reflectarray with 5:1 bandwidth," *IEEE Open J. Antennas Propag.*, vol. 3, pp. 958–969, 2022.

[24] R. Deng, F. Yang, S. Xu, and M. Li, "A 100-Ghz metal-only reflectarray for high-gain antenna applications," *IEEE Antennas Wireless Propag. Lett.*, vol. 15, pp. 178–181, 2016.

[25] X. Cao, C. Deng, Y. Hao, and Y. Yin, "Wideband 3-D printed all-metal reflectarray with notches for low-cost millimeter-wave applications," *IEEE Open J. Antennas Propag.*, vol. 4, pp. 118–125, 2023.

[26] W. Wu, K.-D. Xu, Q. Chen, T. Tanaka, M. Kozai, and H. Minami, "A low-cost wideband reflectarray antenna based on nonradiative dielectric waveguide," *IEEE Antennas Wireless Propag. Lett.*, vol. 22, pp. 3152–3156, 2023.

[27] A. G. Koutinos, G. A. Kyriacou, J. L. Volakis, and M. T. Chryssomallis, "Bandwidth enhancement of antennas designed by band-pass filter synthesis due to frequency pulling techniques," *IET Microw., Antennas Propag.*, vol. 16, no. 1, pp. 1–17, 2022.

[28] A. G. Koutinos, G. A. Ioannopoulos, M. T. Chryssomallis, and G. A. Kyriacou, "A dual-feed rectangular patch antenna for bandwidth enhancement," in *Proc. Loughborough Antennas Propag. Conf. (LAPC)*, 2014, pp. 698–702.

[29] A. G. Koutinos, C. L. Zekios, G. A. Kyriakou, and S. V. Georgakopoulos, "Bandwidth tripling of triangular patch antennas," in *Proc. IEEE Int. Symp. Antennas Propag. USNC-URSI Radio Sci. Meeting (AP-S/URSI)*, 2022, pp. 1772–1773.

[30] A. G. Koutinos, C. L. Zekios, and S. V. Georgakopoulos, "Increasing the bandwidth of wideband antennas using the frequency pulling technique," *IEEE Open J. Antennas Propag.*, vol. 4, pp. 1095–1102, 2023.

[31] C. Exadaktylos, A. G. Koutinos, C. L. Zekios, and S. V. Georgakopoulos, "Increasing the bandwidth of reflectarray antennas using the frequency pulling technique," in *Proc. IEEE Int. Symp. Antennas Propag. USNC-URSI Radio Sci. Meeting (USNC-URSI)*, 2023, pp. 1329–1330.

[32] C. A. Balanis, *Antenna Theory: Analysis and Design*, 4th ed. Hoboken, NJ, USA: Wiley, Feb. 2016.

[33] A. G. Koutinos, C. L. Zekios, S. V. Georgakopoulos, and G. A. Kyriacou, "Increasing the bandwidth of antennas based on the frequency pulling technique: Theoretical limitations and practical considerations," *IEEE Trans. Antennas Propag.*, vol. 72, no. 5, pp. 4064–4076, May 2024.

[34] M. Hamza, C. Exadaktylos, C. L. Zekios, and S. V. Georgakopoulos, "An ultra-wideband fully-planar inverted-l element (FILE) array," *IEEE Trans. Antennas Propag.*, vol. 73, no. 1, pp. 174–187, Jan. 2025.

CHRISTOS EXADAKTYLOS (Graduate Student Member, IEEE) received the Diploma degree in electrical and computer engineering from the Aristotle University of Thessaloniki, Greece, in August 2020. He worked as a Research Assistant with the Aristotle University of Thessaloniki from September 2020 to November 2021. He is currently pursuing the Ph.D. degree with the Transforming Antennas Center, Department of Electrical and Computer Engineering, Florida International University, Miami, FL, USA, under the supervision of Dr. S. V. Georgakopoulos (January 2022–present). His academic interests include phased array technology, ultrawideband antenna arrays, reflectarray, and transmitarray antennas.

ANASTASIOS G. KOUTINOS (Member, IEEE) received the Diploma degree in electrical and computer engineering, the M.S. degree (with Hons.) in electrical and computer engineering communication and satellite telecommunication systems, and the Ph.D. degree (with Hons.) in electrical and computer engineering from the Democritus University of Thrace, Xanthi, Greece, in 2014, 2015, and 2022, respectively. He has been a Postdoctoral Researcher with the Transforming Antennas Center, Florida International University since May 2022. His research is focused on the design of small antennas, bandwidth enhancement techniques, and miniaturization methods for RF devices. His research interests include RF-front-end design, communication and radar systems, and biomedical applications.

CONSTANTINOS L. ZEKIOS (Senior Member, IEEE) received the Diploma degree (Hons.) in electrical and computer engineering, the M.S. degree (Hons.) in electrical and computer engineering communication and satellite telecommunication systems, and the Ph.D. degree (Hons.) in electrical and computer engineering from the Democritus University of Thrace, Xanthi, Greece, in 2008, 2011, and 2015, respectively.

From January 2016 to May 2018, he was a Postdoctoral Researcher with the Department of Electrical and Computer Engineering, University of Massachusetts at Amherst, Amherst, MA, USA. From May 2018 to August 2020, he was a Fellow Postdoctoral Researcher with the Transforming Antennas Center, Florida International University, Miami, FL, USA. From September 2020 to July 2022, he was a Research Assistant Professor with the Department of Electrical and Computer Engineering, Florida International University, where he is currently an Assistant Professor. His main research interests include theoretical and computational electromagnetics, optimization methods, antennas and antenna arrays, electromagnetic surfaces, beamforming networks, microwave engineering, and photonics.

STAVROS V. GEORGAKOPOULOS (Senior Member, IEEE) received the Diploma degree in electrical engineering from the University of Patras, Patras, Greece, in June 1996, and the M.S. and Ph.D. degrees in electrical engineering from Arizona State University, Tempe, AZ, USA, in 1998 and 2001, respectively.

From 2001 to 2007, he was a Principal Engineer with SV Microwave, Inc., West Palm Beach, FL, USA. Since 2007, he has been with the Department of Electrical and Computer Engineering, Florida International University (FIU), Miami, FL, USA, where he is currently a Professor, the Director of the Transforming Antennas Center (a research center on foldable/origami, physically reconfigurable, and deployable antennas), and the Director of the RF Communications, MillimeterWaves, and Terahertz Laboratory. His current research interests relate to novel antennas, arrays, RFID, microwave and RF systems, novel sensors, and wireless powering of portable, wearable, and implantable devices.

Dr. Georgakopoulos received the 2015 FIU President's Council Worlds Ahead Faculty Award, which is the highest honor FIU extends to a Faculty Member for excelling in research, teaching, mentorship, and service. He has served as an Associate Editor for the IEEE TRANSACTIONS ON ANTENNAS AND PROPAGATION from 2013 to 2019. He has been serving as an Associate Editor for the IEEE OPEN JOURNAL OF ANTENNAS AND PROPAGATION since 2019.